Octahedral-shaped perovskite CaCu₃Ti₄O₁₂ with dual defects and coexposed {(001), (111)} facets for visible-light photocatalysis

Reshalaiti Hailili[a], Zhi-Qiang Wang[b], Xue-Qing Gong[b,*], Chuanyi Wang[a,*]

[a] *School of Environmental Science and Engineering, Shaanxi University of Science and Technology, Xi'an, 710021, China*
[b] *Key Laboratory for Advanced Materials, Centre for Computational Chemistry and Research Institute of Industrial Catalysis, School of Chemistry & Molecular Engineering, East China University of Science and Technology, Shanghai, 200237, China*

ABSTRACT

The finite light absorption and rapid charge carrier recombination are two major bottlenecks in semiconductor photolysis. Introducing defects and exposed facets at photocatalysts can significantly improve photoefficiency due to the synergetic effects of extending light response and effective usage of photoinduced charge carriers. However, the prime influential factors in surface defects and predominantly exposed facets that determine photocatalytic performance are still unclear. Herein, to combine the advantages of defects and exposed facets, we, for the first time, report a surfactant-free synthesis and boosted photolysis of a single-crystal CaCu₃Ti₄O₁₂ octahedron with dual defects (oxygen and metal deficiencies of Cu⁺ and Ti³⁺) and coexposed ({001}, {111}) facets by a facile molten salt approach for visible light antibiotic decomposition. The utilized molten salt KCl acts as a structure directing agent, decreasing surface energy to form the octahedron shapes and coexposed facets. As-obtained sample displays a superior efficiency enhancement for antibiotic degradation, approximately 69 times faster than that of its counterpart, defect free CaCu₃Ti₄O₁₂. Density functional theory (DFT) calculations and photodecomposition results show that existing of coexposed facets contributes to spatial separation of carriers, while dual defects improve light absorption, affect charge density and thus promote carrier transfer. The vacancy formation energies of oxygen and titanium defects on exposed facets were calculated. Moreover, dual defects, especially the Ti³⁺ species are greatly affected by defect dipoles of CaCu₃Ti₄O₁₂ with distorted units of CuO₄ and TiO₆, in which TiO₆ clusters make greater contributions on dipole-induced internal field changes. Finally, two concepts of "surface heterojunction" and "defect dipole" are revealed to unveil the synergetic roles of surface chemistry and defect engineering in tuning a photoactivity of crystal based inorganic semiconductors. With dual defects, predominantly coexposed facets and unique crystal shapes, this work reports a strategy and direction for rational synthesis of highly efficient visible light driven catalysts and provides new insights for unearthing the surface chemistry and defect engineering of inorganic photocatalysts.

1. Introduction

Effective charge carrier separation and broadband solar absorption are both important to the solar-driven photocatalytic activity of semiconductors [1,2]. Being regarded as a useful approach, defect chemistry is profoundly crucial to tuning the structure-function property of photocatalysts and has attracted much attention since the surface defects can create new defect levels to influence electronic band structure and facilitate charge carriers (electron and hole) mobility [3–6]. The significance of defect chemistry has triggered intensive studies of the defective catalysts, especially the oxygen vacancy related semiconductors i., TiO₂, BiPO₄, WO₃, ZnO, BiVO₄, Bi₂MoO₆, BiOCl, SrTiO₃ etc [7–14]. Compared to widely studied oxygen vacancies, metal deficiencies were

rarely studied because it is difficult to manipulate the metal defects in robust structured catalysts [3,5]. Thus, an effective approach is highly demanded to investigate the formation of such defects and their distributions to reveal their roles in photocatalytic reactions. Importantly, understanding the correlations of defect-related photocatalytic performance of catalysts is scientifically needed, which could lead to new horizon in the rational design of semiconductors. Although surface defects may improve light absorptions and accelerate effective separation of electron − hole pairs, bulk defects become charge carrier recombination centers and reduce the photocatalytic efficiency [14–16]. Thus, disclosing the roles of surface defects that are capable of facilitating carrier separation, enhancing conductivity and improving photocatalytic performances is a desirable and challenging.

---

* Corresponding authors.
  E-mail addresses: xgong@ecust.edu.cn (X.-Q. Gong), wangchuanyi@sust.edu.cn (C. Wang).

Surface chemistry, especially facet engineering, has attracted great attention due to the fact that the photoinduced electrons and holes can be separated effectively on different exposed facets which can form crystal facet-heterojuctions, where the distinct band gap alignments, and electronic band structure as well as different atomic configuration can modulate the redox potentials of the carriers and provide peculiar reaction sites for the adsorbed molecules to mitigate carrier recombination, thus achieving efficiency enhancement [17,18]. In contrast to heterojunction systems composed of two different compositions, unique crystal facet heterojunctions in a same component allows continuous charge carrier transfer via interface. Due to this reason, facet engineering in various photocatalytic materials with diverse crystal facets for instance., TiO_2, $BiVO_4$, $Au@Ag-Cu_2O$, WO_3, Cu_2O, Ag_3PO_4, BiOCl and $NaTaO_3$ etc. has been developed for efficient solar light harvesting [18–26]. Compared to simple metal oxides such as TiO_2, it is more difficult to manipulate the exposed crystal facets of perovskites, especially in double structured robust photocatalysts. Therefore, the perceptive insight into crystal facet − dependent solar-driven photocatalytic properties still remains intangible.

Considering the advantages of defect chemistry and superiority of characteristic crystal facets on extending light absorption and efficient carrier separation, herein, we report an unprecedented, crystal facet − defect − based double perovskite $CaCu_3Ti_4O_{12}$ consisting of unique octahedron shapes with both dual defects (oxygen and metal vacancies of Cu^+ and Ti^{3+}) and codominant ({001} and {111}) exposed facets by molten salt synthesis. The major contributions of dual defects, exposed facets and carrier separations are understood by DFT investigations and dipole defect analyses. The formation mechanism of octahedrons, dual defects and enhanced efficiency of $CaCu_3Ti_4O_{12}$ is discussed to elucidate the crystal facet − defect − photocatalytic performance correlations. To the best of our knowledge, this is the first example of both dual defects and coexposed facets associated photocatalytic property investigation of double perovskite with unique octahedron shapes.

2. Experimental

2.1. Sample preparation

All chemicals were analytically pure from commercial sources and used without further purification. The target photocatalyst calcium copper titanate was fabricated by one-step molten salt synthesis. In a typical procedure, the stoichiometric mixture of the starting raw materials of metal oxides, e.g., calcium oxide (CaO), copper oxide (CuO) and titanium dioxide (TiO_2, 99.9% purity, Sinopharm Chemical Reagent Co. (SCRC)) were added to the given amount of potassium chloride (KCl, Tianjin Bodi Chemical Industry Co., Ltd.), and then well-grounded for 2 h. The mixture then was heated in the corundum crucible at the temperature of 800 °C by increasing at a rate of 1.0 °C/min and held them for 5.0 h at this temperature to homogenize the melt since the melting point of employed salt potassium chloride was 776 °C. After that, the melt was cooled slowly to room temperature at the rate of 1.0 °C/min. The obtained sample was washed in the mixture of water and absolute ethanol (99.9%) to remove the chlorides, dried at 60 °C for overnight, and then collected for further characterizations and activity evaluations. Yields of as-obtained photocatalyst were ˜ 90%.

As comparison, the defect-free $CaCu_3Ti_4O_{12}$ sample was prepared by a solid-state method, in which stoichiometric quantities of calcium oxide, copper oxide and titanium dioxide (99.9%) were ground thoroughly in an agate mortar for 2 h and the powder mixture was heated at 900 °C for 20 h followed by 800 °C for 8 h with intermittent grinding. After calcination, the samples were grinded, washed with deionized water/ethanol, and then dried at 60 °C, grinded for further characterization.

3. General remarks

X-ray powder diffraction analysis was performed at room temperature using an automated Bruker D8 ADVANCE X-ray diffractometer operating at 40 kV and 30 mA with a scan step width of 0.02° and a fixed counting time of 1 s/step in the angular of 2 θ from 5° to 80° using a diffracted beam graphite monochromator set for Cu Kα (λ = 1.5418 Å). XRD pattern simulation was conducted using Mercury 3.0.17 software for structure comparisons. The microstructures were observed on Field-emission Scanning Electron Microscopy (FESEM, ZEISS SUPRA55VP), which was equipped with EDX G2T20136-5 Energy-Disperse X-ray instrument. Transmission Electron Microscopy (TEM) characterization was performed on a JEOL-JEM 2100 electron microscope. Solid-state optical diffuse reflectance spectrum of per 40.0 mg sample was recorded in a range from 200 nm to 800 nm on a UV–vis spectrophotometer (Shimadzu SolidSpec-3700DUV). The standard $BaSO_4$ powder were employed as 100% reflectance reference. The EPR measurements were conducted on a Bruker E500 instrument operating in the X-band and equipped with an Oxford cryostat at 120 K. Per 30.0 mg of samples were placed in a spectroscopically pure quartz tube (R = 1.5 mm), which was then sent into the EPR cavity with a fixed depth. The g values were determined by calibration with a DPPH (Bruker spectrometer) standard. The XPS measurement was carried out on a VG scientific ESCALAB MK II spectrometer equipped with two ultra-high vacuum (UHV) chambers. All binding energies were calibrated by C 1 s ˜ 284.97 eV. The BET was conducted from the nitrogen adsorption–desorption isotherms recorded by using a Quantachrome Instrument (QUADRASORB IQ). The TOC measurements at a given interval were analyzed on a vario TOC (Elementar, Germany) analyzer. The standard curve was calibrated with potassium hydrogen phthalate solution, and the obtained R value is about 0.9997. The room-temperature photoluminescence (PL) measurement was carried out on a Hitachi F-7000 fluorescence spectrophotometer.

3.1. Assessment of photocatalytic performance

For the photocatalytic activity evaluation, the widely used pharmaceutical resident antibiotic was chosen as a probe molecule. 40.0 mg of sample catalyst was put into a tubular quartz reactor of 100 mL, containing 5.0×10^{-4} mol·L^{-1} of tetracycline aqueous solution, and it was stirred for 30 min, meanwhile kept in the absence of light to attain adsorption equilibrium at room-temperature. A 300 W Xe lamp (PLS-SXE300, Perfect Light Company, Beijing, China) was used as light source. In a typical procedure, the solution (10.0 ml) was sampled at given intervals, then centrifuged and filtered with 0.45 μm filter to discard any sediment. The concentration changes of probe molecule were calculated via a wavelength scan on an UV–vis spectrophotometer (UV–1800, Shimadzu, Japan). The defect-free bulk $CaCu_3Ti_4O_{12}$ was used as a reference material for comparison. The reproducibility and stability of sample during photocatalytic degradation of tetracycline was tested by six cyclic photodecompositions with the same catalyst. For cyclic studies, the catalyst was separated by centrifuging it after the prior cycle and recovered from the centrifuge tube into a beaker with a fresh tetracycline solution. Then, the tetracycline-catalyst contained suspension was subjected to magnetic stirring in the dark and then exposed to visible light irradiation for the next cycle test. To further confirm the stability of sample, the catalyst was filtered and dried for XRD measurement after the reaction.

3.2. Photocurrent response measurement

Photocurrent signal intensity tests were carried out in an electrochemical analyzer (Chenhua Instruments Co., Shanghai). The conventional three-electrodes were used: the ITO/photocatalysts (1 × 1 cm) as the working electrode, a Pt wire as the counter electrode and saturated calomel electrode Ag/AgCl as a reference electrode. The visible light

irradiation is obtained from 300 W Xe lamp. The electrolyte was a 0.1 mol·L^{-1} Na$_2$SO$_4$, which was filled in a single-compartment quart cell.

3.3. Facet-selective photodeposition of Pt

The photo-depositions of reduction deposits on the specific crystal facets of octahedron shaped CaCu$_3$Ti$_4$O$_{12}$ was carried out by using 0.75 mg L^{-1} of H$_2$PtCl$_6$ solution as a precursor and water as a hole trapper, respectively. In a typical procedure, a 50 mg catalyst was dispersed into a 150 ml water with the addition of 1.5 ml H$_2$PtCl$_6$ in a vial, then mixture was exposed to a 300 W Xe lamp, and magnetically stirred for 4 h. After the reaction, the obtained products were separated, and washed with the water/absolute ethanol for several times. Finally, the sample was dried at 60 °C and collected.

3.4. Theoretical investigations

The first-principles calculations were performed using density functional theory (DFT) methodologies implemented in the Vienna ab-initio simulation package (VASP) [27,28]. The generalized gradient approximation (GGA) was used for the exchange of correlation function in a form suggested by Perdew, Burke, and Ernzerhof (PBE) and a cutoff energy of 400 eV was used [29,30]. Electron-ion interactions were treated with the projector augmented wave (PAW) method [31]. The parameter settings in the calculations were as follows: the force criteria on the atoms was less than 0.05 eV/Å, and the energy variation was less than 1×10^{-5} eV per atom. The surface slabs were separated by a vacuum region of 15 Å, which is large enough to prevent the artificial interaction between the distinct slabs. The valence configurations were $4s^2$ for Ca, $3d^{10}4p^1$ for Cu, $4s^13d^3$ for Ti and $2s^22p^4$ for O. Spin-polarized DFT calculations were applied in this study to obtain the lattice parameters, and electronic density of states (DOS) was calculated using a tetrahedron method with Blöchl corrections for (001) and (111). The CaCu$_3$Ti$_4$O$_{12}$ (001) surfaces were modeled by 2-atom-layer slabs which represent 1×1 lateral cells with all atoms were relaxed, and the CaCu$_3$Ti$_4$O$_{12}$ (111) surfaces were modeled by 2-atom-layer slabs which represent 2×2 lateral cells with all atoms being relaxed. In addition, an oxygen atom was removed to model the O$_V$ and titanium atoms was removed to model the Ti$_V$. The energy E$_{vac}$ for forming a vacancy (e.g., oxygen and titanium defects) is defined as:

$$E_{vac} = E_v + 1/2E_{O2} - E_{total} \text{ or } E_{vac} = E_v + E_{Ti} - E_{total}$$

where E$_{total}$ is the calculated total energy of the stoichiometric slab, E$_{O2}$ is the total energy of O$_2$ in gas-phase, E$_{Ti}$ is the energy of titanium atoms, and E$_v$ is the energy of a surface with one vacancy supercell.
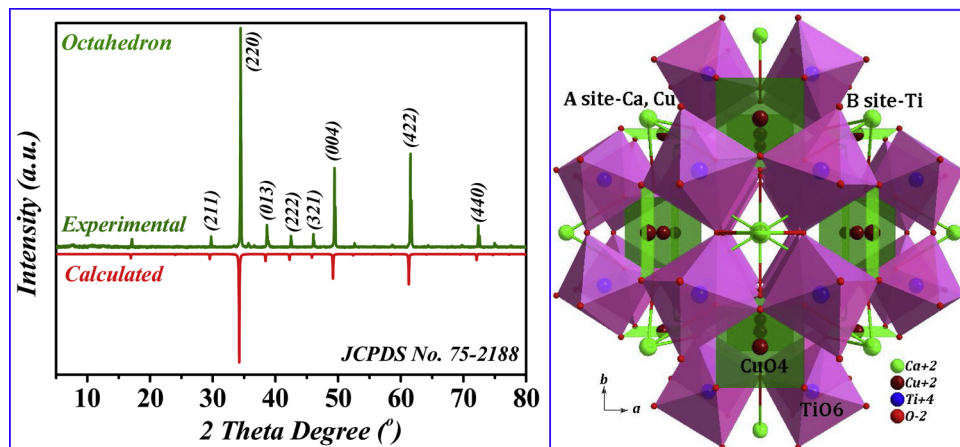
4. Results and discussion

Surface specific is crucial for exploring the structure–property relationships of a photocatalyst, in which photocatalytic activity relates to the exposed crystal facets, morphologies and crystal defects. Generally, all these factors are influenced by preparation methods/conditions. Till now, remarkable progress has been achieved in facet-controlled synthesis with the assistance of capping agents, i.e, F$^-$, H$_2$PO$_4$$^-$, F$^-$/PO$_4$$^{3-}$ by using raw materials e.g., TiCl$_4$, TiCl$_3$ and TiF$_4$ [32–35]. For instance, the predominant {001} facets of TiO$_2$ are usually obtained with the assistance of a shape controlling agent, hydrofluoric acid (HF) [32,33]. However, these precursor/templates are extremely hazardous (corrosive), uneconomic and the reaction process is hard to control due to inevitable hydrolysis. As such, a feasible synthetic method is highly desired. Molten salt synthesis is one of important strategic approaches to prepare photocatalysts with exposed crystal facets and has advantages in facilitating crystal growth with improved phase-purity and homogeneity [36,37]. Thus, the molten salt synthesis was applied in this work. The phase purity of the synthesized sample was identified by XRD characterization and simulation, in which all the as-obtained diffraction peaks match well with the standard phase of CaCu$_3$Ti$_4$O$_{12}$, being consistent with calculated XRD patterns. No other impurities were detected, demonstrating its phase purity (Fig. 1, left). This newly explored photocatalyst is crystallized in *Im-3* (204) space group, exhibiting a double cubic structure. The most remarkable feature of this structure is that its symmetric units are featured with planar tetracoordinated copper containing CuO$_4$ and TiO$_6$ octahedron units (Fig. 1, right), in which Ca and Cu are located on the special places of ABO$_3$ (representing general formula of ideal perovskites). Compared with that of CaCu$_3$Ti$_4$O$_{12}$ prepared by a solid-state method (Fig. S1, in the Supporting Information), relatively higher diffraction peaks can be observed, indicating that high crystallinity is developed during the synthesis. Moreover, the intensities of the (220), (004) and (422) peaks are stronger, implying that there are more exposed facets in the obtained structure.

The SEM image depicts octahedron morphology of the sample obtained in molten salt KCl with specific exposed facets (Fig. 2a), while the comparative CaCu$_3$Ti$_4$O$_{12}$ sample gives very uniform polyhedron shapes (Fig. S2, in the Supporting Information). The EDS images of CaCu$_3$Ti$_4$O$_{12}$ show the phase purity as it only consists of Ca, Cu, Ti and O in the structure (Fig. 2b). The corresponding EDS analysis of reference sample shown in Fig. S3, in the Supporting Information, confirms that the sample prepared by solid-state reaction was CaCu$_3$Ti$_4$O$_{12}$. The observed unique octahedron shapes from TEM images are consistent with exhibited SEM results (Fig. 2). HRTEM images show that the specific distances between two adjacent lattice faults are measured to be 0.1915 nm, 0.2142 nm and 0.2712 nm, agreeing well with the *d*-spacing of (110), (111) and (001) planes, respectively (Fig. 2d), also in
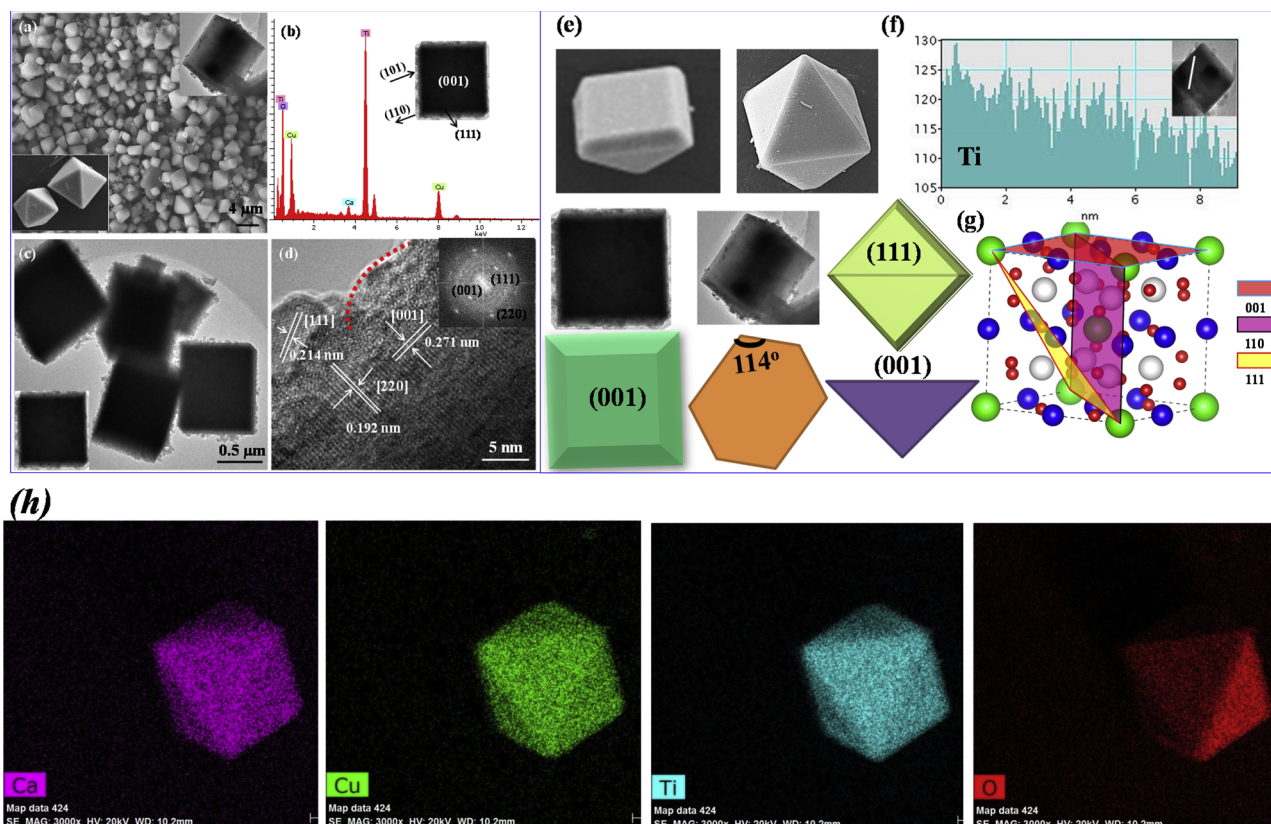

Fig. 1. Experimental and simulated XRD patterns of as-synthesized CaCu$_3$Ti$_4$O$_{12}$ (left, JCPDS card No. 75-2188, *a* = 7.391 Å, cubic), and crystal structure of double perovskite CaCu$_3$Ti$_4$O$_{12}$ in the unit cell (ICSD No. 95714) shows planar CuO$_4$ clusters and TiO$_6$ units along *c* direction (right).

Fig. 2. (a, b) SEM and EDS images of octahedron shaped $CaCu_3Ti_4O_{12}$. Inset (b): observed square from TEM along (001) direction. (c, d) TEM, HRTEM and SAED images of octahedron shaped $CaCu_3Ti_4O_{12}$ crystal. (e) A simple octahedron shape geometrically derived from the unit cell of $CaCu_3Ti_4O_{12}$. (f) Line scan profile of Ti. (g) Different atom distributions on various exposed facets of octahedron shaped $CaCu_3Ti_4O_{12}$. (h) Corresponding elemental mappings of octahedron shaped $CaCu_3Ti_4O_{12}$.

accordance with the XRD results. Same phenomenon was observed in hydrothermally synthesized $PbTiO_3$ with {001} facets, though with the assistance of $K_2Ti_6O_{13}$ nanofibers and mineralized agent $LiNO_3$ during the synthesis [38,39]. Viewing along by the (001) direction, $CaCu_3Ti_4O_{12}$ displays a square shape as depicted in Fig. 2c, in which some dark points are observed, demonstrating that a few precipitated particles from the $CaCu_3Ti_4O_{12}$ nanocrystals are gathered on {111} facets, implying that more electrons are on the {111} facets resulting in migration and separation of electrons and holes to the surface. From the point of crystallography view, it is not surprising to get octahedron shapes since the studied $CaCu_3Ti_4O_{12}$ consists of CuO_4 clusters and TiO_6 units (Fig. 1).

High resolution TEM results of a single octahedron crystal show that the surfaces of sample are not smooth, and the edges become more disordered (Fig. 2d), indicating the generation of certain defects. It was articulated that such a high abundant lattice disorder in semiconductors can produce mid-gap states, which are quite different from defect energy distributions in single crystals. Moreover, small rhombus facets were observed at the corner of this square arranged crystal and can be defined as high-index facets of {110} based crystal structures (in the inset Fig. 2b and e). It can be argued from the lattice images of inner and edges of octahedron obtained from TEM results that the prepared sample is in single crystalline character and acquires high uniformity i.e., as supported by Ti profiles and elemental mapping images in Fig. 2f and h, respectively. On the basis of aforementioned analyses and crystal structures, the {101} and {110} are flat facets, thus it can be confirmed that the prepared octahedron shaped crystal predominant mainly consists of two representative coexposed facets of {001} and {111}, respectively. Moreover, it can be seen from crystal structure and TEM analysis that, only five-coordinated Ti (Ti 5c) atoms and Cu atoms are present on the (001) surface, while {111} facets are mainly composed

with Cu atoms and O 3c (Fig. 2g). Obviously, {001} facets acquire favorable atomic structure, on which large amounts of Ti 5c can become active sites by adsorbing/capturing anions such as Cl^- than that of {111} facets.

Acquiring relatively low melting point, flux agents or molten salts, e.g., KCl (melting point 776 °C), could reduce the calcination temperature, thus accelerating the ion substitution and electrostatic interaction on specific surface. Herein, we assume, anions (Cl^-) from molten salt KCl are adsorbed onto the crystal facets and incline to minimize the surface energy of {001} facets, resulting in rapid decreases of {001} crystal facets and relatively faster growth of {111} facets. On the basic level, these atoms with low surface energy prove to be the most stable and grow slowly to generate exposed facets. Previous theoretical and experimental investigations demonstrate that halogen anions like F^-, Cl^- and Br^- can reduce surface energy of {001} facet in $BiVO_4$, CuO and TiO_2 [19,23,33]. Therefore, it can be concluded that Cl ions from the melting salt is one of the crucial factors for generating exposed facets and octahedron shapes of $CaCu_3Ti_4O_{12}$. Same results were observed in {001} exposed faceted-TiO_2, in which formation of these exposed facets was ascribed to the role of F^- from HF [33]. However, we provide surfactant (template) free synthesis of perovskites with coexposed ({001}, {111}) facets. The preparation and formation procedures of octahedron shaped $CaCu_3Ti_4O_{12}$ crystal are illustrated in Scheme 1.

The optical properties of octahedron and polyhedron shaped $CaCu_3Ti_4O_{12}$ (obtained from molten salt and solid-state reactions, respectively) were analyzed by UV–vis diffuse reflectance spectral (DRS) measurements. As-obtained samples can absorb light with a wavelength onset respectively at 409 nm and 589 nm, the results of which are demonstrated in Fig. 3a. The corresponding optical band gaps are estimated to be 3.031 eV and 2.110 eV, converted by the Kubelka–Munk
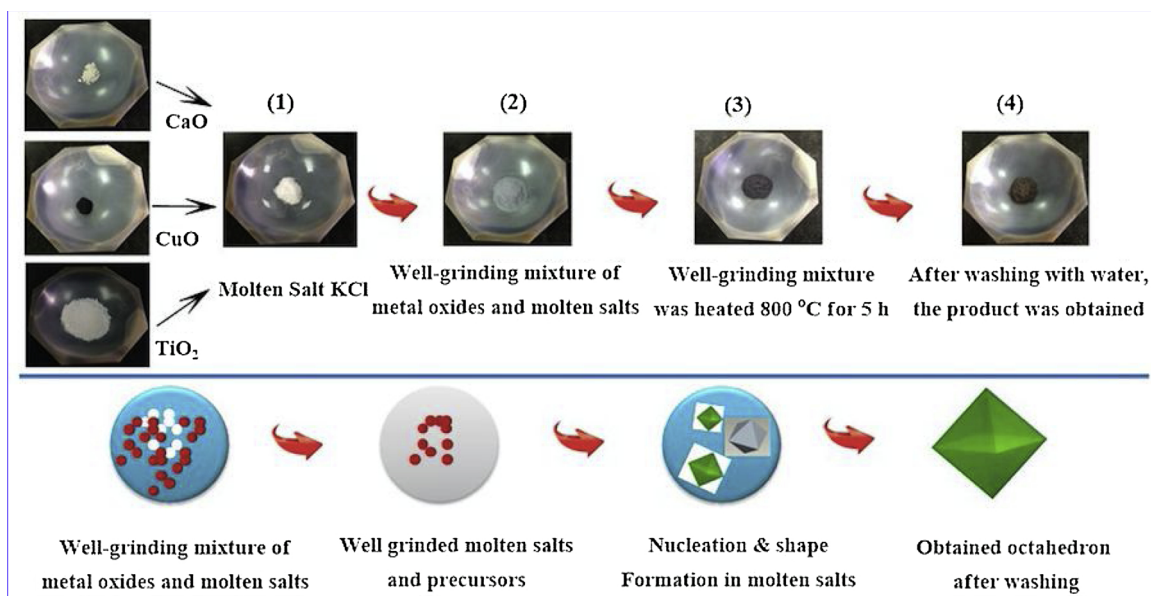
Scheme 1. The process of molten salt synthetic approach for octahedron shaped CaCu₃Ti₄O₁₂.

function, indicating potential visible-light photocatalytic activity [40]. First-principle density functional theory (DFT) calculations of CaCu₃Ti₄O₁₂ demonstrate that its valence band is comprised of Cu 3d and O 2p states, which leads to a narrower band gap in compared to commonly studied photocatalysts of TiO₂ (~ 3.210 eV, anatase) and CaTiO₃ (~ 3.760 eV), for which the valence bands are mainly composed of O 2p orbitals [41,42]. The observed strong and broad light absorptions at around 300 nm–360 nm are attributed to the electron excitation from the valence band to the conduction band of Ti unoccupied 3d orbitals in TiO₆, while the observed light absorptions in the range of 600–800 nm are corresponding to the Cu^{2+} d–d transitions. As depicted in Fig. 3a, the light absorptions give significant decrease and tailed up to 600 nm in octahedron shaped crystal, meanwhile the broad and strong light absorptions around 450 nm–600 nm implying existence of defects such as oxygen deficiency or metal imperfections. The presence of surface disorder (Fig. 2d)indicates reduced Ti^{4+}, which would be beneficial for the generation of surface Ti^{3+} species and oxygen vacancies. These defects are the prime factors resulting in narrower band gap, and improved light absorption. However, additional reliable characterizations are needed to be verify the existence and distribution of such surface defects.

Low-temperature electron paramagnetic resonance (EPR) measurements were carried out to confirm whether synthesized samples possess defects (Fig. 3b). The observed EPR signals at around the *g* value of 1.982 can be assigned to the characteristic peaks of Ti^{3+} ($3d^1$) [7]. In CaCu₃Ti₄O₁₂, presence of Ti^{3+} species can disrupt Ti—O—Ti bonds in a

TiO₆ cluster resulting in local electrical polarization. From the view point of crystal structure of CaCu₃Ti₄O₁₂, Ca and Cu atoms are highly incorporated in the A sites of the ABO₃, where Cu is connected with for oxygen atoms to display [CuO₄] clusters and bonded with [TiO₆] units with one oxygen atom. Thus, either distortion of clusters (TiO₆ or CuO₄) or Ti displacement in TiO₆ units are directly affect the crystal structures and generate imperfections, i.e., Ti^{3+} or copper–oxygen defects from the [CuO₄]' and [CuO₄]" units [43,44]. As predicted, the characteristic isotropic signal at around the *g* value of 2.077 was observed in octahedron, and can be assigned to unpaired electrons trapped on copper − oxygen vacancy (Fig. 3b) [45]. The electron transformations of $Cu^{2+} + e^- \rightarrow Cu^+$, $Ti^{4+} + e^- \rightarrow Ti^{3+}$ require opposite species for instance oxygen vacancy O^{2-} for a charge balance. As a result, the plane defects in CuO₄ are formed, and will in turn, generate slightly distorted TiO₅ square in the structure, where the TiO₅ clusters are composed with Ti^{4+} and Ti^{3+}. Significantly, step by ionization of molten salt provides enough reaction times and chance for the ion assembling of Ti−O−Ti lattice, and as a result the metal deficiency is generated. These captured defects could adsorb/activate O₂ molecules to form superoxide anions ($^•O_2^-$), of which the corresponding EPR signal appears at about $g \sim 2.046$ (Fig. 3b) [45]. As comparison, the EPR measurement of polyhedron shaped CaCu₃Ti₄O₁₂ was carried out, in which no significant EPR signals were captured (described as defect free CaCu₃Ti₄O₁₂), further demonstrating the existence of high abundant dual defects in CaCu₃Ti₄O₁₂ octahedron (described as dual defective CaCu₃Ti₄O₁₂) as depicted in Fig. 3b. Existing defects usually induces the

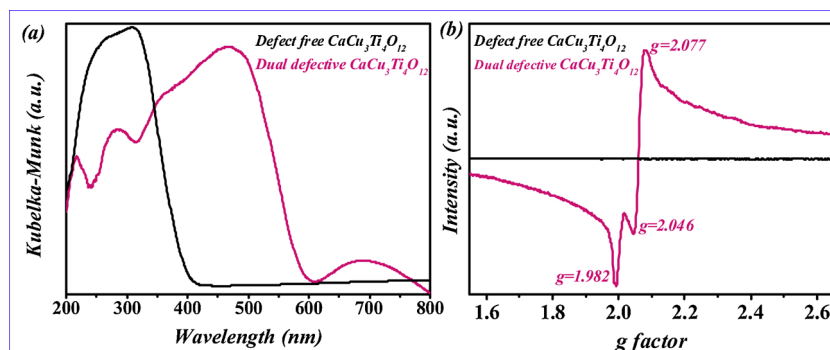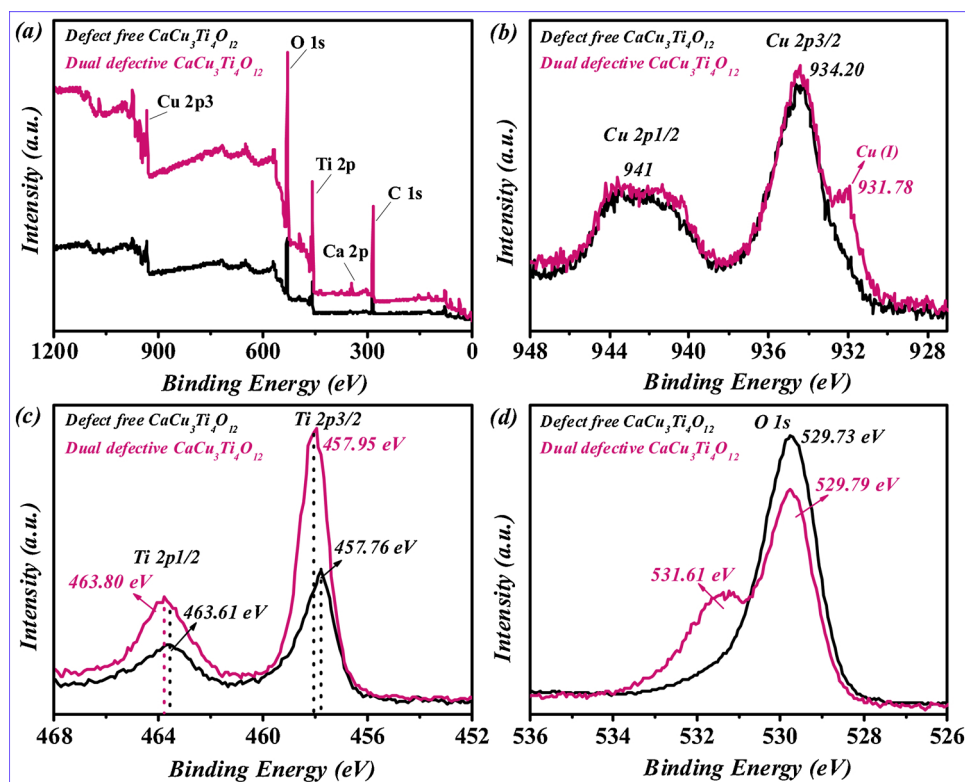**Fig. 3.** (a) Comparison of room-temperature UV–vis DRS spectra and (b) Low–temperature EPR signals of as-obtained CaCu₃Ti₄O₁₂ samples.

Fig. 4. XPS spectra of (a) the overall survey, (b) Cu 2p, (c) Ti 2p, and (d) O 1 s on the dual defective and defect free $CaCu_3Ti_4O_{12}$.

change of valence state because the electrons or holes can be transferred to the atoms neighboring the defects. It is worth to mention that metal defects are easily formed in the catalysts with high abundant oxygen vacancy, formation of which coexists with the Ti^{3+} and Cu^+ generation in order to make charge compensation. To confirm chemical states of the elements and defects in the $CaCu_3Ti_4O_{12}$, XPS analysis was carried out.

Fig. 4a shows the whole-range spectra, demonstrating the presence of Ca, Cu, Ti and O. For both samples of dual defective and defect free $CaCu_3Ti_4O_{12}$, three composed elements (Cu, Ti and O) with different chemical states are verified by XPS, and the corresponding high-resolution spectra in the energy range of Cu 2p, Ti 2p and O 1 s signals are represented in Fig. 4b–d, respectively. The corresponding binding energies for Cu peaks are at around 934.20 eV and 941.17 eV, representing Cu $2p_{3/2}$ and Cu $2p_{1/2}$ peaks for characteristic Cu (II) in both dual defective and defect free $CaCu_3Ti_4O_{12}$ (Fig. 4b) [20]. Furthermore, the shake-up satellites in the 937–945 eV range are also the characteristic of Cu (II), while a shoulder peak with binding energy of 931.90 eV is attributed to Cu (I) in dual defective octahedron shaped $CaCu_3Ti_4O_{12}$. As CuO was used as starting materials for the synthesis, the nominal valence charge of Cu atoms in sample should be +2 though the XPS spectra reveal that Cu (I) presents in dual defective octahedron, which is consistent with the observed EPR results. In fact, the valence charge of Cu is perturbed by defect induced oxygen vacancies as confirmed by XPS spectra. Two broad peaks at around 457.76 eV and 463.61 eV with weak signal intensities are observed in defect free $CaCu_3Ti_4O_{12}$, while relatively strong peaks of about 457.95 eV and 463.80 eV are detected in dual defective octahedron, can be ascribed to the characteristic energies of Ti $2p_{3/2}$ and Ti $2p_{1/2}$, respectively [46]. As shown in Fig. 4c, these observed peaks can be attributed to oxygen vacancy related Ti^{3+}, suggesting that the concentrations of Ti^{3+} on the surface of both dual defective and defect free sample are rich though with different intensities, in consistence with the observed EPR results (Fig. 3b). As can be seen from Ti 2p profiles of dual defective octahedron, the peak positions varies by 0.19 eV and the

whole XPS peaks are shifted, implying the shift of Fermi level in dual defective sample. It is plausible because defect (Ti^{3+} species or oxygen vacancies) generation would affect the electron density distributions and induce new electronic states formation, thus push the Fermi level upward, which will be discussed in the section of clarification of photocatalytic mechanism. Besides, effective charge transfer between metals ($Ti^{4+} + Cu^{2+} \rightarrow Ti^{3+} + Cu^{3+}$) could prevent further oxidation of Ti^{3+} by surface adsorbed O_2 molecules into Ti^{4+} ($Ti^{3+} + O_2 \rightarrow Ti^{4+} + \cdot O_2^-$) and rapid generation of more $\cdot O_2^-$ radicals in dual defective octahedron, resulting in broad and high XPS characteristic peaks of oxygen defects (Fig. 4d). The O 1 s profiles of samples are shown in Fig. 4d, in which very strong and broad peaks at around 529.73 eV and 529.79 eV were observed both in defect free and dual defective $CaCu_3Ti_4O_{12}$, while 531.61 eV was observed only in dual defective octahedron. The O 1 s peaks at about ˜ 529.73 eV corresponds to the oxygen ions (O^{2-}) in defect free sample, while ˜ 0.06 eV peak shift for dual defective octahedron $CaCu_3Ti_4O_{12}$ might be ascribed to the interaction of defects with hydroxyls. The captured XPS peak of 531.61 eV can be assigned to the formation of oxygen defects. Thus, it can be assumed form the EPR and XPS results that the metal deficiencies (Ti^{3+}) and oxygen vacancies coexist in dual defective octahedron shaped $CaCu_3Ti_4O_{12}$, and formation of these species might be ascribed to the role of stepwise ionization of utilized molten salt.

It has been demonstrated that photocatalysts with crystal imperfections and predominantly exposed facets showed significant roles both in optical responses and photocatalytic performances, which strongly depend on the surface property, electronic structures and atomic configurations of photocatalysts, especially with visible light illumination. Thus, it is reasonable to speculate that acquiring dual defects and coexposed facets, the octahedron would cause drastic changes in a photocatalytic activity that has not previously been reported.

Effective treatment of pharmaceutical residuals is one of the most meaningful topics as these hazards would cause environment pollution [47]. Based on unique structure of octahedron shapes, predominant
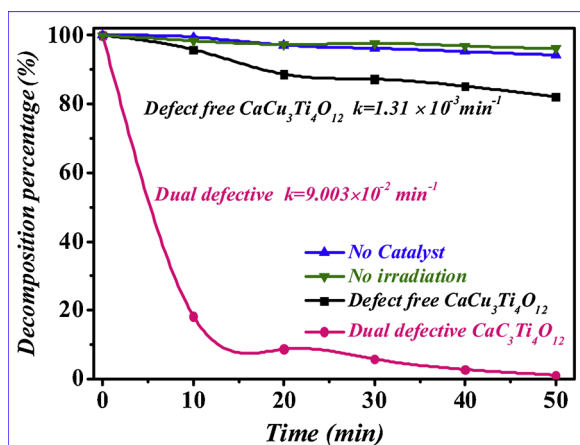
Fig. 5. Comparison visible light degradation ratio and corresponding apparent rate constants (k) of tetracycline in the presence of octahedron shaped dual defective and defect free $CaCu_3Ti_4O_{12}$.

coexposed crystal facets, dual defects and excellent optical absorption capabilities, the visible light driven photocatalytic activity of $CaCu_3Ti_4O_{12}$ for an antibiotic (tetracycline, Fig. S4, in the Supporting Information) degradation was interrogated. The experimental results of visible-light photocatalytic decomposition of tetracycline over $CaCu_3Ti_4O_{12}$ crystals are shown in Fig. 5. No significant degradation was observed in the absence of either catalyst or light irradiation, suggesting that above parameters are significantly important for decomposition processes. The residual concentration of tetracycline in aqueous solution decreases to a certain extent upon prolonging the irritation time. The decomposition results show that the reaction efficiency becomes higher with the utmost percentage of 99.34% tetracycline disintegration merely with 50 min visible light illumination. The relevant data for the polyhedron shaped defect free $CaCu_3Ti_4O_{12}$ was investigated as reference.

The surface characters of a catalyst are primarily significant on the photocatalytic activity as a photocatalytic reaction occurs on its surface. The specific nitrogen adsorption-desorption isotherms and the corresponding pore size distributions of the representative samples were measured as shown in Fig. S5 (in the Supporting Information), respectively. The BET surface area of octahedron shaped $CaCu_3Ti_4O_{12}$ was determined to be $8.42 \, m^2 \, g^{-1}$, nearly 2.86 times larger than that of defect free one ($\sim 2.94 \, m^2 \, g^{-1}$), indicating that the specific surface area of samples increases accompanied by the employing molten agents with moderate reaction conditions. The enlargement of surface area of dual defective octahedron giving a narrow distribution of the mesopores at ~ 8.41 nm can be ascribed to the well-defined octahedron structures with specific edges and facets. The larger the surface areas are, in general, the higher the photocatalytic efficiencies.

The kinetics of the photodegradation of tetracycline is analyzed according to equation: $\ln(C_o/C) = kt$ [48]. Linear correlation between $\ln(C_o/C)$ and reaction interval (t) indicates that the tetracycline decomposition obeys the rules of first-order kinetics. The apparent rate constant k (min^{-1}) of dual defective $CaCu_3Ti_4O_{12}$ octahedron is $9.003 \times 10^{-2} \, min^{-1}$, approximately 68.73 times faster than that of tetracycline degradation over defect free $CaCu_3Ti_4O_{12}$ ($1.31 \times 10^{-3} \, min^{-1}$). When the first-order rate constants k were normalized to their surface areas, a relatively higher efficiency was observed in dual defective octahedron shaped $CaCu_3Ti_4O_{12}$ of about $1.06 \times 10^{-2} \, g \, min^{-1} \, m^{-2}$, about 24 times higher than that of defect free one ($4.45 \times 10^{-3} \, g \, min^{-1} \, m^{-2}$). The higher rate constant normalized to surface area might be attributed to the dual defects, predominantly exposed facets and small bang gap of dual defective octahedron shaped $CaCu_3Ti_4O_{12}$, which can be easily excited, and render it effective formation of carriers. Approximately 92.57% reduced total

organic carbon (TOC) was achieved over dual defective $CaCu_3Ti_4O_{12}$, implying successful degradation of a probe molecule (Fig. S6, in the Supporting Information). The decomposition percentages display no obvious differences even after 300 min visible light irradiation, while the crystal structures before and after the reaction basically retain unchaged as evidenced by XRD results (Fig. S7 and S8, in the Supporting Information), indicating exceptional efficiency and outstanding stability of the dual defective $CaCu_3Ti_4O_{12}$ octahedron. With 99.34% decomposition, 92.57% reduced TOC and larger normalized apparent rate constant ($1.06 \times 10^{-2} \, g \, min^{-1} \, m^{-2}$), the dual defective octahedron *is* a potential visible light driven materials with pronounced activity and robust structure.

For the better understanding and underlying of the cooperative mechanism involved in a superior photocatalytic performance of dual defective octahedron shaped $CaCu_3Ti_4O_{12}$ crystal, several factors such as effective carrier separation and charge transfer, characteristic exposed facets, dual defects and nature of geometric structure as well as defect dipoles are analyzed.

4.1. (i) Dual defects induced charge carrier separation and transfer are important factors

The foremost step in photocatalytic reaction is the formation of electron–hole pairs upon light irradiation, required to be separated and migrated to the catalyst's surface, where photoinduced electrons and holes invoke subsequent redox reactions. Thus, the successful generation of carriers is a prerequisite for effective photolysis.

The formation of photoinduced carriers and charge transfer in dual defective $CaCu_3Ti_4O_{12}$ octahedron are analyzed by comparing its band edge positions with the redox potentials of various active species. The corresponding band edge position was determined using equation of $E_{CB} = \chi - E_C - 0.5E_g$ and $E_{VB} = E_g - E_{CB}$, where E_{CB}, χ, E_C, E_g and E_{VB} are the CB potentials, absolute electronegativity of the composed elements, band gap energy and valence band potentials, respectively [49,50]. Compared with the large electronic band gap of 3.03 eV in defect free $CaCu_3Ti_4O_{12}$ with the valence band VB (E_{VB}) maximum at 2.62 eV and the conduction band CB (E_{CB}) minimum at -0.411 eV, our dual defective octahedron shaped $CaCu_3Ti_4O_{12}$ displays relatively narrower band gap of 2.094 eV with the E_{VB} maximum at 2.165 eV (vs NHE), which is more positive than $E°(OH^-/\cdot OH) = 1.99$ eV, vs NHE at pH = 7.0 (Fig. 6a) [51]. Notably, the CB minimum of representative sample is about 0.051 (vs, NHE) not suitable for superoxide generation since it is more positive than that of thermodynamics of $E°(O_2/\cdot O_2^-) = -0.046$ eV. However, electron transfer between metals Ti^{4+}/Ti^{3+} (-0.498 eV vs. NHE) could react with surface-adsorbed O_2 molecules, thus generating $\cdot O_2^-$ radicals ($Ti^{3+} + O_2 \rightarrow Ti^{4+} + \cdot O_2^-$) due to the strong reduction capabilities of Ti^{3+} ions [44,52]. Moreover, the differentiations in the E_{CB} minimum and E_{VB} maximum resulted from the Ti^{3+} related oxygen vacancies, are favorable for electrons and holes transportation from bulk to the surface of the catalysts. Given the quite reasonable thermodynamics, the photocatalytically active radicals e.g., electrons (e^-), holes (h^+), hydroxyl radicals ($\cdot OH$) and superoxide anions ($\cdot O_2^-$) could be generated upon the visible light irradiation and invoke redox reaction or directly oxidize tetracycline. Thus, a good compatibility between the absorption of visible light and the redox abilities were obtained for samples with suitable band structures, thus giving rise to a significantly enhancement in photoefficiency for organic pollutants decomposition.

The captured defects such as oxygen vacancy and, Ti^{3+} provide active sites to trap/consume electrons to produce more superoxide radicals ($\cdot O_2^-$) together with the synergetic roles of coexposed facets that can separate electron–hole pairs and reduce their recombination rates. Moreover, the VB of $CaCu_3Ti_4O_{12}$ comprises of Cu 3d + O 2p and its optical property mainly arises from charge carrier transition from a ground state to an excited state. The presence of oxygen vacancies and Ti^{3+} would enhance charge transfer occupying distinct crystallographic
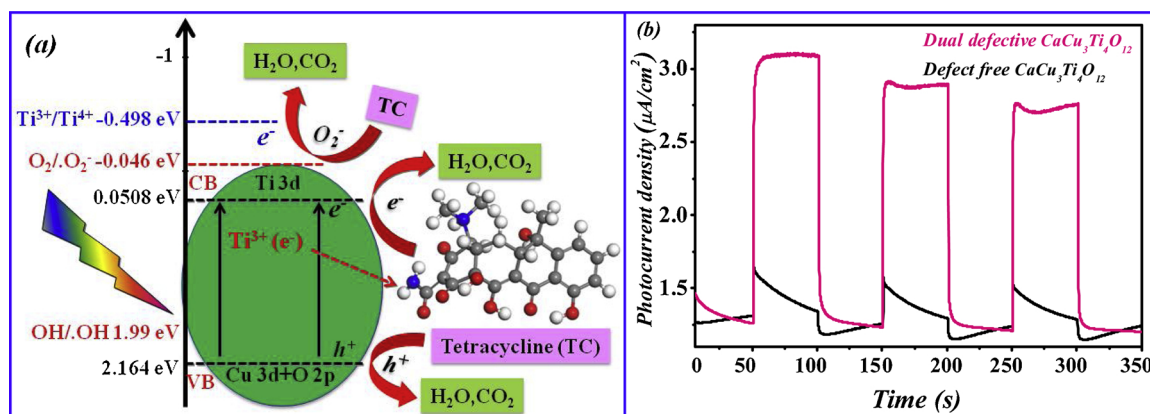
Fig. 6. (a) Effective production of electron–hole pairs over dual defective octahedron. (b) Comparative photocurrent response of dual defective and defect free $CaCu_3Ti_4O_{12}$.

sublattices to generate photoactive electrons to increase the electron donor density, promote depletions of photoinduced carriers, and accelerate charge transportations due to the strong redox capabilities of active species such as electrons or $\cdot O_2^-$ anions (generated via the reduction of surface adsorbed O_2 by electron transfer between metals), and thus charge carrier separation was successfully achieved. Same results of enhanced carrier separations from $\cdot O_2^-$ generation were observed in $Ti^{4+}-O-Fe^{2+}-Ti^{3+}-O-Fe^{3+}$, $Ti^{4+}-O-Fe^{2+}$, $Ti^{4+}-O-Ce^{3+}$ and $Ti^{4+}-O-Cu^+$ systems, in which CB also consists of Ti 3d [52–54]. Importantly, increasing Ti^{3+} species in the structure could enhance electron conductivity, carrier mobility and charge carrier separation as supported by PL study (Fig. S9, in the Supporting Information). In order to further reveal the electron transfer/separation capability of studied samples, the photoelectrochemical activity was analyzed by transient photocurrent measurements. The photocurrent signals were observed by continuously switching off and on at given time. The corresponding photocurrent density of dual defective $CaCu_3Ti_4O_{12}$ octahedron is $0.085\,mA\cdot cm^{-2}$, approximately 10.3 times as high as that of defect free sample under visible light irradiation (Fig. 6b). Thus, the improved photolysis was originated from the charge transfer and surface defects. Besides, characteristic exposed facets may contribute to improved efficiency.

4.2. (ii) Characteristic coexposed facets ({001}, {111}) are relevant for enhanced photolysis

To thoroughly investigate the influences of characteristic coexposed {001} and {111} facets of dual defective $CaCu_3Ti_4O_{12}$ octahedron on effective carrier transfer and separation, the energy band levels and density of states (DOS) of two different surfaces were calculated by DFT (Fig. 7). After the alignment with respect to electronic levels of a bulk sample, the CBM of $CaCu_3Ti_4O_{12}$ (001) was found to be higher than that of $CaCu_3Ti_4O_{12}$ (111) by ~ 0.49 eV. Therefore, it is expected that the photogenerated electrons would transfer from the {001} facets to the {111} in CBM, while holes migrate in opposite direction from the {111} facets to the {001} in VBM. Herein, it can be deduced from the above calculation results that the facet heterojuction structures can be formed due to the energy level differences between CB and VB levels of the exposed {001} and {111} facets. Notably, upon successive visible light irradiation, photoinduced electrons on the {001} surface will transfer to the exposed facets of {111} because the different band gap alignments and differences in energy levels in these two exposed facets. As a result, the number of electrons on the {111} facets will be increased and preferred as reduction sites resulting in effective separation with holes since photoinduced holes simultaneously accumulate on {001} facets and serving as oxidation sites. Thus, different crystal facets have specific oxidation–reduction capabilities and the electrons and holes can be

spatially separated in dual defective octahedron shaped $CaCu_3Ti_4O_{12}$ by isolated reduction and oxidation sites. Following these spontaneous circulations of carrier separations on assorted exposed facets, carrier recombination will be reduced, and its reverse reaction can be prevented.

The selective photoreduction deposition test was carried out by deposing Pt to experimentally prove the spatial separation of photoinduced carriers and its transfer pathway on assorted coexposed facets of a dual defective $CaCu_3Ti_4O_{12}$ octahedron (Fig. 8). After deposition, the {001} facets of octahedron shaped $CaCu_3Ti_4O_{12}$ are remain bare except for trace amounts of nanoparticles on these surfaces, while nearly all the edges of octahedron shaped $CaCu_3Ti_4O_{12}$ are fully covered with redox deposits as depicted in Fig. 8a–f. These results suggested that photoinduced electrons are easily gathered on {111} facets, and the holes are mostly on {001} facets for reduction reactions, implying spatial separation of photoinduced electron–hole pairs, as supported by our DFT calculations of band edge positions (Fig. 7). It should be pointed out that photogenerated electrons on the {111} exposed facets are available for photoreduction reaction, though also can act as reaction sites for molecular oxygen activation to generate much more stronger oxidants such as superoxide radicals or hydrogen peroxide species during the photolysis. Based on the crystal structure of $CaCu_3Ti_4O_{12}$, it can be observed that a greater proportion of {001} polar facets are mostly titanium-terminated, while the {111} facets are mainly composed with copper and oxygen atoms, which are all favorable to interactions and improved adsorption of tetracycline. Additionally, with greater proportions of unsaturated Ti (five-coordinated Ti), and Cu-terminated atomic arrangement (Fig. 2g), the {001} exposed facets contribute to promote the photocatalytic reaction as these large amounts of Ti 5c can become active sites [55]. Therefore, superior photocatalytic performance might be ascribed to its {001} and {111} predominant coexposed facets of dual defective octahedron shaped $CaCu_3Ti_4O_{12}$.

As revealed by theoretical investigation in our previous study, the oxygen vacancies are produced and become stable in $CaCu_3Ti_4O_{12}$ due to the easy breaking of metal-oxygen bonds [45,55]. Moreover, existing oxygen deficiencies also affect the charge distributions as a result of $Cu^+ + O_2 \rightarrow Cu^{2+} + \cdot O_2^-$, which is favorable for tetracycline decomposition. Importantly, in the $CaCu_3Ti_4O_{12}$ crystal, the positions of oxygen atoms in main composed units of TiO_6 or CuO_4 control the bond angles, charge states and atom arrangements. For example, variations of the $Cu-O$ bond length in the CuO_4 cluster directly affect the distortion/tilting degree of TiO_6 by changing the crystal structure and generate defects. These defects also affect the charge distributions and enhance donor density leading to charge transportations and efficiency improvement. The electron spin density maps for defect free and dual defective $CaCu_3Ti_4O_{12}$ on the crystal surfaces of {001} and {111} were
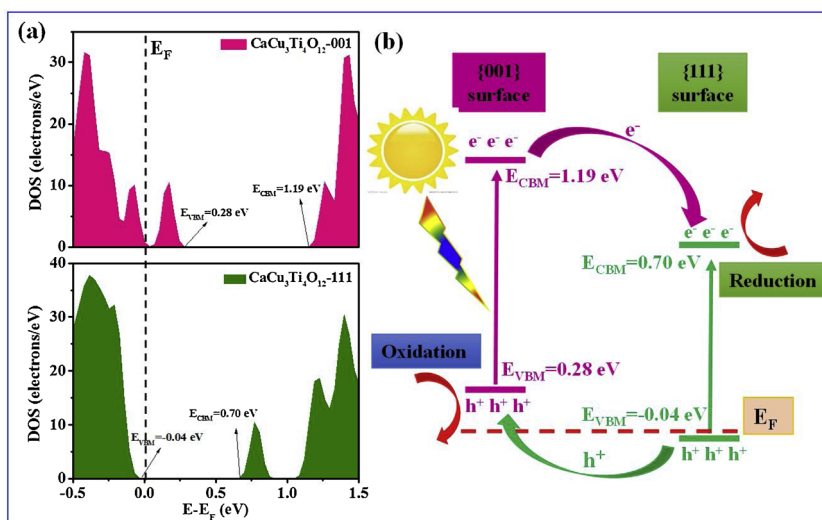
Fig. 7. Calculated partial density of states: (a) {001} and {111} surfaces of CaCu$_3$Ti$_4$O$_{12}$, and (b) the relative positions of the key states of the {001} and {111} facets of CaCu$_3$Ti$_4$O$_{12}$.

analyzed (Fig. 9), and it can be found that the spin electrons prefer to localize on Cu 3d–O 2p states, mainly on Cu atoms (Cu^{2+} → Cu$^+$). This is also the prime reason for CaCu$_3$Ti$_4$O$_{12}$ to exhibit the relatively narrower band gap (Cu 3d–O 2p). The defect states are localized on Cu 3d–O 2p states and oxygen vacant sites.

Actually, presence of localized Cu$^+$ reduces electron mobility in the CB (Ti 3d) and accelerates carrier recombination while electron mobility would have increased with Ti^{3+} species [44]. However, captured Ti^{3+} is able to reduce surface adsorbed oxygen at the surface to generate superoxide radicals, which provides the possibility for carrier transformations between Ti^{3+} and Cu$^+$ sites and will in turn decrease the defect concentrations of Cu$^+$. The Table 1 shows the formation

energy of oxygen and titanium vacancy. The oxygen vacancy formation energy in {001} is much lower than that in {111} as the corresponding formation energies are calculated to be 0.90 eV and 2.03 eV, respectively. On the contrary, very interesting results are obtained on the formation energy of titanium defects, in which the higher vacancy generation energy is observed in {001} with the value of 11.38 eV, nearly 1.321 times higher than that of formation energy on {111} facets. However, the defect formation energies on different exposed facets ({001}, {111}) of CaCu$_3$Ti$_4$O$_{12}$ have never been reported, to the best of our knowledge.

The reconstruction of the specific surface would take place when the defect exists on the surface. Notably, as shown in Fig. 10, the CBM
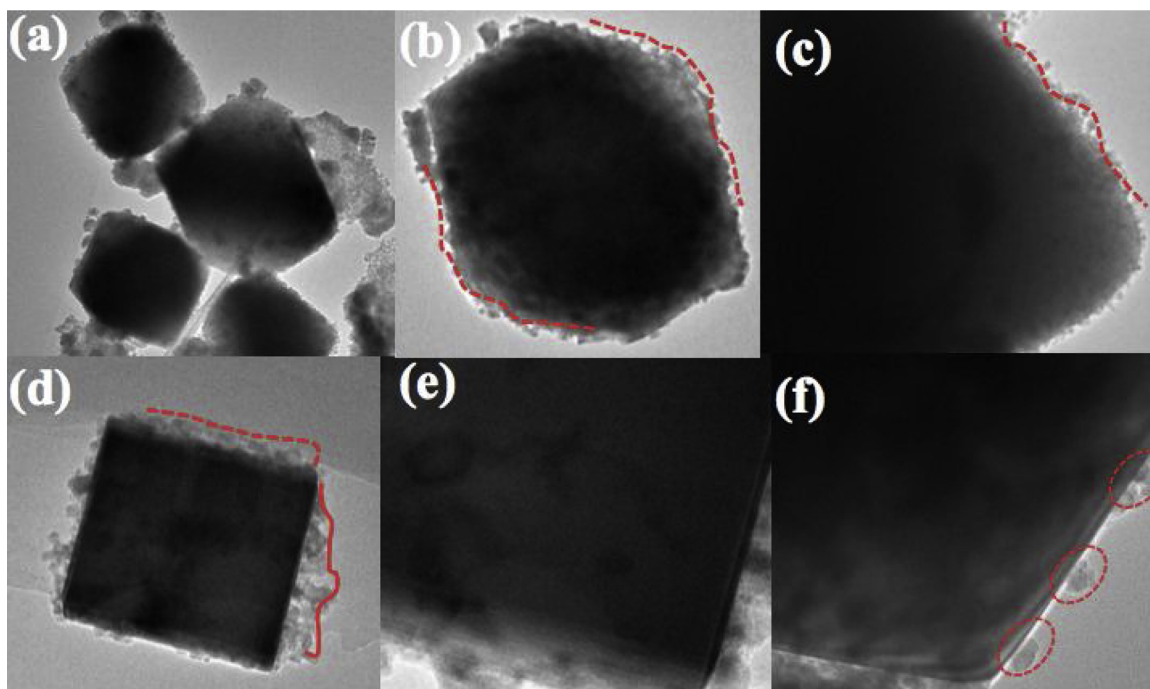

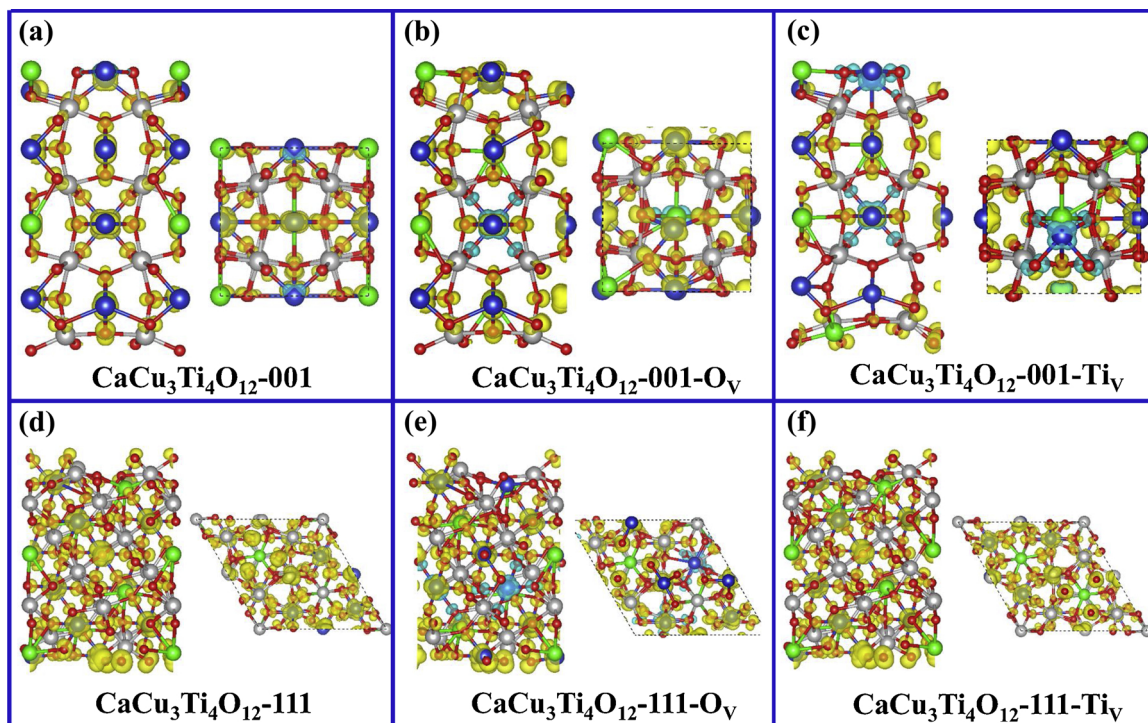**Fig. 8.** TEM images of selective photoreduction deposition of Pt on the surface of dual defective octahedron shaped CaCu$_3$Ti$_4$O$_{12}$.

Fig. 9. Calculated electron spin density contours for the defect free and dual defective $CaCu_3Ti_4O_{12}$ with {001} and {111} coexposed facets. Atoms in the ball-and-stick mode are color-coded as: green, Ca; brick red, Cu; gray, Ti; red, O. Spin up density contours color is yellow, and spin down is blue.

Table 1
The oxygen and titanium vacancy formation energy on (001) and (111) surface of the $CaCu_3Ti_4O_{12}$.

Exposed facets	E_{vac}-O_V (eV)	E_{vac}-Ti_V (eV)
$CaCu_3Ti_4O_{12}$-001	0.895	11.375
$CaCu_3Ti_4O_{12}$-111	2.025	8.575

would move to the Fermi level when the oxygen defects exist (E_{CBM} = 0.91 eV to 0.81 eV) and the VBM would move far away from the Fermi level (E_{VBM} = 0.0 eV to 0.16 eV) with the presence of titanium deficiencies on the (001) surface of $CaCu_3Ti_4O_{12}$, which means that the VB width increases, quite consistent with the observed XPS results. The detailed DOS calculations of $CaCu_3Ti_4O_{12}$ with specific defects and coexposed crystal facets are given in the Fig. **S10**, in the Supporting Information. However, the VB width intrinsically controls mobility of the photoinduced holes and wider VB results in higher mobility of holes. Herein, the presence of vacancies makes the electrons to be more easily excited into the CB under solar irradiation, thus leading to the higher photoconversion efficiency.

4.3. (iii) Dual defects and geometric structures are the significant factors for enhanced photolysis

The surface defects and nature of its surface-interface property are also taken into account. From the structural point of view, as a main framework of $CaCu_3Ti_4O_{12}$, the TiO_6 units not only determine the electrooptical property, but also associate with diverse defects (i., oxygen and metal vacancy) and would tilted by CuO_4 units showing low symmetry of Ti^{4+} compared with that of simple perovskites ABO_3. The unsaturated atoms from oxygen defects in the dual defective octahedron can offer catalytically active sites for antibiotic adsorptions, while the dual defects will significantly decreases the symmetry of cubic structure to form polarization by internal field changes resulting efficiency enhancement. Herein, observed dual defects not only increase the electrical conductivity, but enhance charge carrier mobility because oxidation of dual metal defects of Cu^+ and Ti^{3+} binding with surface adsorbed oxygen molecules, decreases the concentrations of bulk oxygen defects to generate superoxide anions via $Ti^{3+} + O_2 \rightarrow Ti^{4+} + \cdot O_2^-$ and $Cu^+ + O_2 \rightarrow Cu^{2+} + \cdot O_2^-$. On the other hand, presence of oxygen defects could act as electron trapping sites for free carriers, resulting in shift of positive charge center, and thus enlarging atomic spacing between adjacent Ti defects and shortening the distance
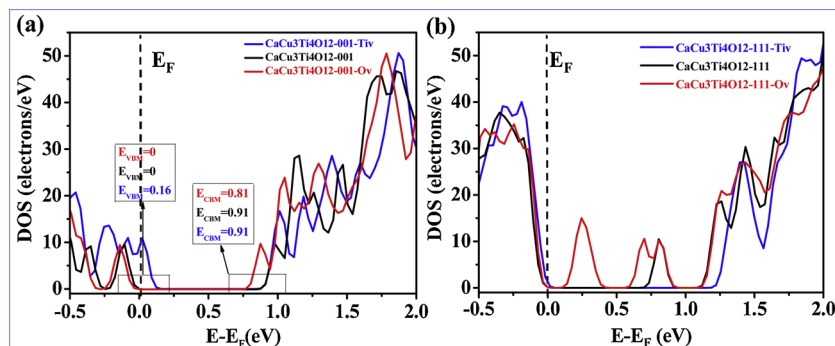

Fig. 10. Calculated density of states of defect free and dual defective octahedron shaped $CaCu_3Ti_4O_{12}$ with specific defects on the coexposed crystal facets of (a) {001} surfaces, and (b) {111} surfaces, respectively. The blue line is for $CaCu_3Ti_4O_{12}$ surfaces with a Ti vacancy, the black line for $CaCu_3Ti_4O_{12}$ surfaces, and the red line for $CaCu_3Ti_4O_{12}$ surfaces with a O vacancy (For interpretation of the references to colour in this figure legend, the reader is referred to the web version of this article).

Table 2

Magnitude Debye of polyhedra in the asymmetric unit of $CaCu_3Ti_4O_{12}$ and TiO_2.

Species		Direction				Dipole Moment	
		x (a)	y (b)	z (c)	Magnitude Debye		Total (esu·cm/Å³)
CaCu3Ti4O12	Ti1O6 (x, y, z)	$-4.9 \times 10-15$	$-7.5 \times 10-15$	0	0		0
	TiVO6 (x, y, z)	2.593	-3.46017	-12.33	13.059		0.06436
	CuO4 (x, y, z)	0	$1.07 \times 10-14$	0	0		0
	CuVO3 (x, y, z)	-7.528	-6.857	0	10.182		0.05018
TiO_2 (Anatase)	Ti1O6 (x, y, z)	0	-7.859	0	7.8591		0.0212
TiO_2 (Rutile)	Ti1O6 (x, y, z)	0	0	0	0		0

between other adjacent atoms to generate defect dipoles in the structure. The relatively high polarizations of various units play an important role in interfiled changes and is beneficial for the carrier separation according to Inoue's study [56]. In $CaCu_3Ti_4O_{12}$, missing of any oxygen atoms in TiO_6 frameworks or CuO_4 clusters affects the structures in the unit cell, leading to distortion and consequently the inter field changes. Thus, the higher the oxygen defects, the stronger distortion degree. To further elucidate the effect of defects, electron distributions to the entire units cell of $CaCu_3Ti_4O_{12}$, the dipole moments were calculated.

The local dipoles of crystallographically independent units of CuO_4 and TiO_6 in $CaCu_3Ti_4O_{12}$ is calculated according to Debye equation: $\mu = neR$, where μ is a dipole moment, n is the electrons, e representing charges, R is the varied charges [57]. This method has been used to calculate the distortion of MoO_6 and TeO_x polyhedra in $BaTeMo_2O_9$, acentric $MoO_3F_3^{3-}$ anions in $Ag_3MoO_3F_3$, and TiO_n/PbO_n polyhedra in $Pb_2Bi_4Ti_5O_{18}$, etc. and well explain the experimental results [57–59]. In the defect free bulk $CaCu_3Ti_4O_{12}$, the dipole moments of CuO_4 and TiO_6 are almost close to zero, demonstrating that these two units are nearly free from distortion, and thus display a relatively poor photocatalytic performance. It is very interesting to find that the octahedral TiO_6 units with one missed one oxygen atoms give dipole moments of 13.059 D, while CuO_4 unit with the one copper oxygen vacancy displays approximately 10.182 D dipole moment in the structure. Compared with the calculation results of dipole variation in star photocatalyst TiO_2, it can be deduced that the oxygen vacancies in the TiO_6 have greater impact on electronic interfiled changes of $CaCu_3Ti_4O_{12}$ than that of copper oxygen defects in CuO_4 clusters, even higher than that of dipole moments in perfect TiO_6 units in anatase TiO_2 (7.859 D). The detailed calculation results are given in Table 2. Such drastic internal field changes are beneficial for trapping the photoinduced holes and thus the carrier separations can be enhanced.

On the other hand, the oxygen vacancies will directly influence the framework of octahedron structure and missing of any oxygen atoms in two polyhedron units (TiO_6 and CuO_4) affects the crystal structure, electron densities as well as redistribution of charges on every atoms, and need to adsorb organic pollutant or small molecular in order to keep the charge balance. The curtail step of photocatalytic reaction, effective surface adsorption, is invoked from photocatalyst's surface and its inherent defects. Thus, the enhanced photoactivity of dual defective octahedron is originated from structure-induced variations by dual defects and spatial separations of coexposed facets, which are significant to reveal structure-property correlations in defect engineering and surface chemistry. To date, unique octahedron shaped dual defective double perovskites with highly predominant coexposed facets has scarcely been explored.

5. Conclusions

In summary, we have successfully developed an unprecedented, crystal facet-based octahedron shaped $CaCu_3Ti_4O_{12}$ with ({001}, {111}) coexposed facets and dual defects (oxygen vacancies and metal defect of Cu^+ and Ti^{3+}) by a one-step molten salt synthesis. The followings are highlighted in this contribution:

i This is the first example of octahedron shaped $CaCu_3Ti_4O_{12}$ with dual defects (oxygen vacancy and metal defect) and predominant coexposed ({001}, {111}) facets. The utilized salt KCl is not only found to be crucial for defect manipulations, but the Cl ions from KCl can also minimize the surface energy of specific facets, by which growth directions of the {001} and {111} can be tuned;

ii Dual defective and defect free $CaCu_3Ti_4O_{12}$ display visible light photoactivities for antibiotic degradation, in which dual defective sample exhibits much higher efficiency enhancement, (approximately 68.73 times faster) than its counterpart, defect free $CaCu_3Ti_4O_{12}$;

iii Density functional theory (DFT) calculations and photodecomposition results showed that existing of exposed facets contribute to spatial separation of electron − hole pairs. The DFT and dipole moment calculations revealed that dual defects have vital influences on crystal structure and charge density distributions. The vacancy formation energies of oxygen and titanium defects on different exposed ({001}, {111}) facets were calculated for the first time. Moreover, dual defects, especially Ti^{3+} related oxygen deficiency greatly affect defect dipoles of $CaCu_3Ti_4O_{12}$ by creating dipole-induced internal field changes and promote carrier transformations/separations;

iv Based on the experimental and theoretical results, two concepts of "surface heterojunction" and "defect dipole" are disclosed to elucidate the pivotal roles of surface chemistry and defect engineering in the photocatalytic activity of crystal based inorganic photocatalysts. The boosted photocatalysis in $CaCu_3Ti_4O_{12}$ is attributed to effective charge carrier separations induced from the synergetic roles of dual defects, codominant exposed facets and defect dipoles.

This work not only provides a facet engineering strategy to improve photoconversion efficiency, but it also adequately exemplifies the fundamental understanding of preparation and unveiling the correlations between surface chemistry and defect engineering by revealing the morphology-crystal facet-defect-performance of inorganic perovskite catalysts.

Appendix A. Supplementary data

Supplementary material related to this article can be found, in the online version, at doi:https://doi.org/10.1016/j.apcatb.2019.03.086.

References

[1] R.G. Li, F.X. Zhang, D.G. Wang, J.X. Yang, M.R. Li, J. Zhu, X. Zhou, H.X. Han, C. Li,

Nat. Commun. 2401 (2013) 1–7.
[2] L.C. Mu, Y. Zhao, A.L. Li, S.Y. Wang, Z.L. Wang, J.X. Yang, Y. Wang, T.F. Liu, et al., Energy Environ. Sci. 9 (2016) 2463–2469.
[3] S. Bai, N. Zhang, C. Gao, Y.J. Xiong, Nano Energy 53 (2018) 296–336.
[4] J.K. Stolarczyk, S. Bhattacharyya, L. Polavarapu, J. Feldmann, ACS Catal. 8 (2018) 3602–3635.
[5] J. Nowotny, M.A. Alim, T. Bak, M.A. Idris, M. Ionescu, K. Prince, M.Z. Sahdan, K. Sopian, M.A.M. Teridi, W. Sigmund, Chem. Soc. Rev. 44 (2015) 8424–8442.
[6] S.M. Wu, X.L. Liu, X.L. Lian, G. Tian, C. Janiak, Y.X. Zhang, Y. Lu, H.Z. Yu, J. Hu, H. Wei, H. Zhao, G.G. Chang, G. Van Tendeloo, L.Y. Wang, X.Y. Yang, B.L. Su, Adv. Mater. 30 (2018) 1802173.
[7] X.B. Chen, L. Liu, P.Y. Yu, S.S. Mao, Science 331 (2011) 746–749.
[8] Y.Y. Zhu, Q. Ling, Y.F. Liu, H. Wang, Y.F. Zhu, Appl. Catal. B 187 (2016) 2014–2211.
[9] N. Zhang, X.Y. Li, H.C. Ye, S.M. Chen, H.X. Ju, D.B. Liu, Y. Lin, W. Ye, C.M. Wang, Q. Xu, F.F. Zhu, L. Song, J. Jiang, Y.J. Xiong, J. Am. Chem. Soc. 138 (2016) 8928–8935.
[10] M.-H. Liu, Y.-W. Chen, X.Y. Liu, J.-L. Kuo, M.-W. Chu, C.-Y. Mou, ACS Catal. 6 (2016) 115–122.
[11] H. Li, F. Qin, Z.P. Yang, X.M. Cui, J.F. Wang, L.Z. Zhang, J. Am. Chem. Soc. 139 (2017) 3513–3521.
[12] S. Gao, B.C. Gu, X.C. Jiao, Y.F. Sun, X.L. Zu, F. Yang, W.G. Zhu, et al., J. Am. Chem. Soc. 139 (2017) 3438–3445.
[13] H. Li, J. Shang, H.J. Zhu, Z.P. Yang, Z.H. Ai, L.Z. Zhang, ACS Catal. 6 (2016) 8276–8285.
[14] X.H. Chen, S.N. Choing, D.J. Aschaffenburg, C.D. Pemmaraju, D. Prendergast, T. Cuk, J. Am. Chem. Soc. 139 (2017) 1830–1841.
[15] Y.F. Ji, Y. Luo, J. Am. Chem. Soc. 138 (2016) 15896–15902.
[16] X.C. Jiao, Z.W. Chen, X.D. Li, Y.F. Sun, S. Gao, W.S. Yan, C.M. Wang, Q. Zhang, Y. Lin, Y. Luo, Y. Xie, J. Am. Chem. Soc. 139 (2017) 7586–7594.
[17] Q.L. Chen, Y.Y. Jia, S.F. Xie, Z.X. Xie, Chem. Soc. Rev. 45 (2016) 3207–3220.
[18] H.G. Yang, C.H. Sun, S.Z. Qiao, J. Zou, G. Liu, C.S. Smith, H.M. Cheng, et al., Nature 453 (2008) 638–641.
[19] R.G. Li, F.X. Zhang, D. Wang, J.X. Yang, M.R. Li, J. Zhu, X. Zhou, H.X. Han, C. Li, Nat. Commun. 4 (2013) 1432.
[20] K.-H. Yang, S.-C. Hsu, M.H. Huang, Chem. Mater. 28 (2016) 5140–5146.
[21] C. Yang, Z.M. Yang, H.W. Gu, C.K. Chang, P. Gao, B. Xu, Chem. Mater. 20 (2008) 7514–7520.
[22] S.Y. Bao, Z.Q. Wang, X.Q. Gong, C.Y. Zeng, Q.F. Wu, B.Z. Tian, J.L. Zhang, J. Mater. Chem. A 4 (2016) 18570–18577.
[23] W.X. Huang, Acc. Chem. Res. 49 (2016) 520–527.
[24] Y.P. Bi, S.X. Ouyang, N. Umezawa, J. Cao, J.H. Ye, J. Am. Chem. Soc. 133 (2011) 6490–6492.
[25] Z.G. Yi, J.H. Ye, N. Kikugawa, T. Kako, S.X. Ouyang, H.S. Williams, H. Yang, J.Y. Cao, W.J. Luo, Z.S. Li, Y. Liu, R.L. Withers, Nat. Mater. 9 (2010) 559–564.
[26] Q. Zhang, Z. Li, S.Y. Wang, R.G. Li, X.W. Zhang, Z.X. Liang, H.X. Han, et al., ACS Catal. 6 (2016) 2182–2191.
[27] G. Kresse, J. Furthmüller, Comput. Mater. Sci. 6 (1996) 15–50.
[28] G. Kresse, J. Furthmüller, Phys. Rev. B 54 (1996) 11169.
[29] J.P. Perdew, Y. Wang, Phys. Rev. B 45 (1992) 13244–13249.
[30] J.P. Perdew, K. Burke, M. Ernzerhof, Phys. Rev. Lett. 77 (1996) 3865–3868.
[31] P.E. Blöchl, Phys. Rev. B 50 (1994) 17953–17979.
[32] M. Liu, L.Y. Piao, L. Zhao, S.T. Ju, Z.J. Yan, T. He, C.L. Zhou, W.J. Wang, Chem. Commun. (Camb.) 46 (2010) 1664–1666.
[33] H.G. Yang, G. Liu, S.Z. Qiao, C.H. Sun, Y.G. Jin, S.C. Smith, J. Zou, H.M. Cheng, G.Q. Lu, J. Am. Chem. Soc. 131 (2009) 4078–4083.
[34] Y.B. Zhao, Y.F. Zhang, H.W. Liu, H.W. Ji, W.H. Ma, C.C. Chen, H.Y. Zhu, J.C. Zhao, Chem. Mater. 26 (2014) 1014–1018.
[35] S.W. Liu, J.G. Yu, M. Jaroniec, J. Am. Chem. Soc. 132 (2010) 11914–11916.
[36] L.H. Li, J.X. Deng, J. Chen, X.R. Xing, Chem. Sci. 7 (2016) 855–865.
[37] L.H. Li, J.X. Deng, J. Chen, X.Y. Sun, R.B. Yu, G.R. Liu, X.R. Xing, Chem. Mater. 21 (2009) 1207–1213.
[38] S.Q. Deng, G. Xu, H.W. Bai, L.L. Li, S. Jiang, G. Shen, G.R. Han, Inorg. Chem. 53 (2014) 10937–10943.
[39] S.M. Yin, H. Tian, Z.H. Ren, X. Wei, C.Y. Chao, J.Y. Pei, X. Li, G. Xu, G. Shen, G.R. Han, Chem. Commun. 47 (2011) 6763–6783.
[40] P. Kubelka, F. Munk, Z. Technol. Phys. 12 (1931) 593–601.
[41] L. Kavan, M. Gra1tze, S.E. Gilbert, C. Klemenz, H.J. Scheel, J. Am. Chem. Soc. 118 (1996) 6716–6723.
[42] H.J. Zhang, G. Chen, Y.X. Li, Y.J. Teng, Int. J. Hydrog. Energy 35 (2010) 2713–2716.
[43] M.-H. Whangbo, M.A. Subramanian, Chem. Mater. 18 (2006) 3257–3260.
[44] J.H. Clark, M.S. Dyer, R.G. Palgrave, C.P. Ireland, J.R. Darwent, M.J. Rosseinsky, J. Am. Chem. Soc. 133 (2011) 1016–1032.
[45] X.J. Luo, Y.S. Liu, C.P. Yang, S.S. Chen, S.L. Tang, K. Bärner, J. Eur. Ceram. Soc. 35 (2015) 2073–2081.
[46] X.M. Yu, B. Kim, Y.K. Kim, ACS Catal. 3 (2013) 2479–2486.
[47] H. Wang, H. Yao, P. Sun, D. Li, C.H. Huang, Environ. Sci. Technol. 50 (2016) 145–153.
[48] J.M. Buriak, P.V. Kamat, K.S. Schanze, ACS Appl. Mater. Interfaces 6 (2014) 11815–11816.
[49] R.G. Pearson, Inorg. Chem. 27 (1988) 734–740.
[50] Y. Xu, M.A.A. Schoonen, Am. Mineral. 85 (2000) 543–556.
[51] P.M. Wood, Biochem. J. 253 (1988) 287–289.
[52] R. Hailili, Z.-Q. Wang, M.Y. Xu, Y.H. Wang, X.-Q. Gong, T. Xu, C.Y. Wang, J. Mater. Chem. A 5 (2017) 21275–21290.
[53] T.-H. Xie, X.Y. Sun, J. Lin, J. Phys. Chem. C 112 (2008) 9753–9759.
[54] R. Nakamura, A. Okamoto, H. Osawa, H. Irie, K. Hashimoto, J. Am. Chem. Soc. 129 (2007) 9596–9597.
[55] R. Hailili, Z.-Q. Wang, Y.X. Li, Y.H. Wang, K.S. Virender, X.-Q. Gong, C.Y. Wang, Appl. Catal. B 221 (2018) 422–432.
[56] J. Sato, H. Kobayashi, K. Ikarashi, N. Saito, H. Nishiyama, Y. Inoue, J. Phys. Chem. B 108 (2004) 4369–4375.
[57] H. Zhang, H. Wang, Y. Xu, S.F. Zhuo, Y.F. Yu, B. Zhang, Angew. Chem. Int. Ed. 51 (2012) 1459–1463.
[58] I.D. Brown, D. Altermatt, Acta Crystallogr. Sect. B Struct. Sci. B41 (1985) 244–247.
[59] R. Hailili, G.H. Dong, S. Jin, C.Y. Wang, T. Xu, Ind. Eng. Chem. Res. 56 (2017) 2908–2916.